PIER C

Quasi-Monomode Resonator for Ka-Band Applications

Vadym Pazynin[1], Asel Begimova[2], Nursaule Burambayeva[2],
Kostyantyn Sirenko[3, *], Nataliya Yashina[3], and Wilhelm Keusgen[1]

[1] *Technical University of Berlin, Berlin, Germany*
[2] *L.N. Gumilyov Eurasian National University, Astana, Kazakhstan*
[3] *O.Ya. Usikov Institute for Radiophysics and Electronics, National Academy of Sciences of Ukraine, Kharkiv, Ukraine*

ABSTRACT: The paper presents a model of an open resonator exhibiting a single high-Q eigen oscillation within a one-octave frequency band. The resonator is synthesized by integrating a diffraction radiation antenna, which comprises a segment of a dielectric waveguide above a metal substrate with a diffraction grating, into a system of flat reflectors aligned parallel to the wave fronts of surface and bulk waves generated by the antenna. A pulse response with an amplitude-frequency characteristic featuring one pronounced resonant maximum, which corresponds to an eigen oscillation with Q factor exceeding 10^4, has been achieved in the proposed system. The optical length of the resonator exceeds the wavelength of the working oscillation by over 50 times. The feasibility of tuning the resonator via moving both the mirrors and the diffraction grating is demonstrated. The proposed model holds promise for applications in the development of solid-state and quantum radiation sources operating in the microwave and higher frequency ranges.

1. INTRODUCTION

Quasi-optical open resonators (ORs) find their use in various applications where the electromagnetic wavelength is less than 1–2 cm. The primary challenge in designing such ORs is the undesirable proliferation of eigen oscillations as the working oscillation's volume-to-wavelength ratio increases. This can lead to situations where numerous eigen oscillations of the resonator overlap in frequency, causing the OR to lose its frequency selectivity. Reducing the number of eigen oscillations in ORs is a pressing concern, prompting the exploration of various strategies. These include insertion of scattering inhomogeneities into the OR field [1–5], utilization of dielectric coatings [6], incorporation of multilayer dielectric inserts in the OR cavity [7], utilization of external cavities [8, 9], deployment of frequency-selective elements [10–14], and others. However, no universal solution exists, and each particular case demands a specific technique. A significant hurdle in addressing this challenge is the presence of several undesired modes alongside the primary operating oscillation in the spectral characteristics of ORs.

In this paper, we present a model of an OR operating on a single high-Q eigen oscillation within one-octave frequency band. The OR's operation relies on the spatial-frequency selection of waves of an open transmission line (in this case, it is a segment of dielectric waveguide) positioned adjacent to a diffraction grating (Fig. 1). This waves selection occurs due to the interaction between the field of an open waveguide and a diffraction grating. As a result, the incoming waveguide wave undergoes either complete or partial transformation into a bulk wave, which is then radiated into open space. The radiation angle depends on the frequency and geometrical parameters of the grating. This phenomenon is the wave analog of the well-known
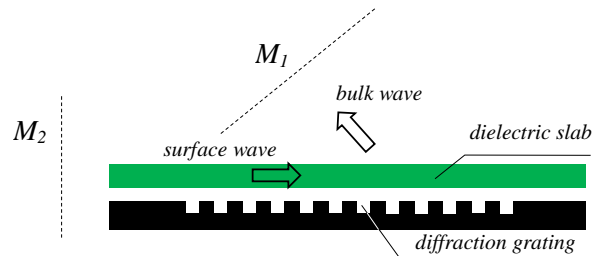

FIGURE 1. Diffraction radiation antenna.

Smith-Purcell effect, but is reciprocal in nature [15–18]. Consequently, it enables the construction of diffraction radiation antennas capable of both transmission and reception regimes [16, 19–25].

To synthesize the OR, we employ the reciprocity principle. Placing two mirrors, M_1 and M_2 (see Fig. 1), parallel to the wave fronts of surface and bulk waves enables the cyclic motion of the energy, leading to the formation of a standing wave. In this system, the diffraction grating acts as a frequency-selective reflector, imposing stringent conditions on partial waves that could form a standing wave of the working oscillation. These conditions pertain to the radiation angle, frequency, and proportion of the energy emitted by the grating during a single pass along the resonator (radiator efficiency). Alongside the general requirement that the optical size of the resonator must match an integer number of half-wavelengths, these conditions effectively filter out a substantial portion of oscillations that might otherwise be excited in a resonator of this size. Despite the apparent simplicity of construction, such a resonator in principle, its practical realization, even as a numerical model, demands the resolution of numerous optimization and fine-tuning challenges at the component level. In this paper, we present the

---

* Corresponding author: Kostyantyn Sirenko (k.sirenko@gmail.com).

results of model synthesis of such an OR operating in the Ka band.

2. PROBLEM FORMULATION AND NUMERICAL APPROACH

In our numerical experiments, we employed the method of exact absorbing conditions (EACs) [26–32], a particularly suitable choice for time-domain modeling of resonant devices as it remains accurate even in long-duration simulations. The name EACs owes its origin to the use of exact conditions on virtual boundaries that truncate an unbounded domain of interest. Outgoing waves pass through virtual boundaries with EACs without any reflection or distortion, as if they are absorbed by these boundaries. The essence of this method is the mathematically rigorous EACs and the proved equivalence of initial boundary value problems on unbounded and truncated domains [26–29]. In contrast to the widely adopted perfectly matched layers (PMLs), EACs stand on a solid mathematical foundation [30–32]. In this work, the EAC-enabled finite-difference time-domain (FDTD) method [27–29] is employed, although other alternatives are also feasible [32].

Let us consider a 2D initial boundary value problem for E-polarized fields. In the Cartesian coordinate system, the electric and magnetic fields vectors $\vec{E}$ and $\vec{H}$ have only three nonzero components: $E_x = E_x(y, z, t)$, $H_y = H_y(y, z, t)$, and $H_z = H_z(y, z, t)$. The analysis domain $\mathbf{Q_L}$ (see Fig. 2) is a portion of the Cartesian plane $\{y, z\}$, which is enclosed by the rectangular virtual boundary $\mathbf{L}$ and the virtual boundaries $\mathbf{L_1}$ and $\mathbf{L_2}$ in the cross-sections of semi-infinite waveguide ports [27–29]. The formulation of this initial boundary value problem is as follows:

$$
\begin{cases}
\eta_0 \dfrac{\partial H_y}{\partial t} = -\dfrac{\partial E_x}{\partial z}, \ \eta_0 \dfrac{\partial H_z}{\partial t} = \dfrac{\partial E_x}{\partial y}, \ \dfrac{\varepsilon}{\eta_0}\dfrac{\partial E_x}{\partial t} = \dfrac{\partial H_z}{\partial y} - \dfrac{\partial H_y}{\partial z}, \\
t \geq 0, \quad g \equiv \{y, z\} \in \mathbf{Q_L}, \\
E_x(g, 0) = H_y(g, 0) = H_z(g, 0) = 0, \\
\partial E_x(g, 0)/\partial t = \partial H_y(g, 0)/\partial t = \partial H_z(g, 0)/\partial t = 0, \\
E_x(g, t)\big|_{g \in \mathbf{M}} = 0, \\
E_x^{(1)}(g, t)\big|_{g \in \mathbf{B}} = E_x^{(2)}(g, t)\big|_{g \in \mathbf{B}}, \\
H_{tan}^{(1)}(g, t)\big|_{g \in \mathbf{B}} = H_{tan}^{(2)}(g, t)\big|_{g \in \mathbf{B}}, \\
\int\limits_V (\varepsilon E_x^2 + \mu(H_y^2 + H_z^2))dV < \infty, \\
\dfrac{\partial u_n(z, t)}{\partial z} = \mp \dfrac{\partial u_n(z, t)}{\partial t} \mp \lambda_n \int\limits_0^t u_n(z, \tau) K_n(t - \tau)d\tau, \\
E_x^{out,m}(g, t)\big|_{g \in \mathbf{L_m}} = \sum\limits_{n=1}^{\infty} u_n^{out,m}(z, t)\big|_{\mathbf{L_m}} \cdot \mu_n(y), \\
E_x^{inc,1}(g, t)\big|_{g \in \mathbf{L_1}} = u_n^{inc,1}(z, t)\big|_{\mathbf{L_1}} \cdot \mu_n(y), \\
\mathbf{A_L}\big[E_x(g, t)\big]_{g \in \mathbf{L}} = 0.
\end{cases}
\tag{1}
$$

Here, the first line is the Maxwell equations; the second line sets the areas of definition of the independent variables y, z, and t; the third and fourth lines outline the initial conditions; the fifth, sixth, and seventh lines are the boundary conditions on perfectly conducting surfaces ($\mathbf{M}$) and interfaces between dielectric objects ($\mathbf{B}$); and the eighth line prescribes the conditions on the edges of metal and dielectric scatterers $\mathbf{V}$ (where V denotes the finite volume encompassing the edge $\mathbf{V}$). It is followed by the EACs for space-time amplitudes $u_n(z, t)$
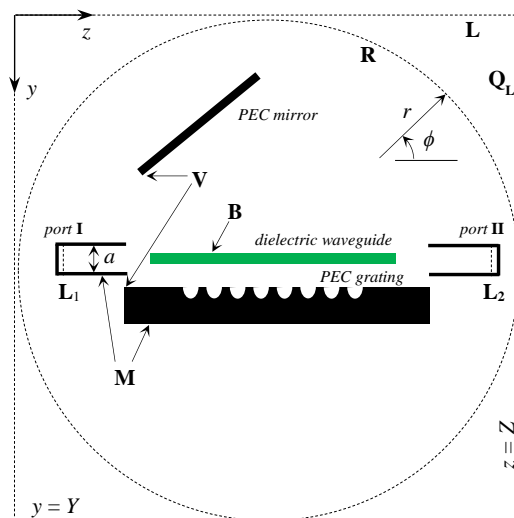

FIGURE 2. Generalized layout of the analysis domain and object under study.

[28, 29] of outgoing $(u_n(z, t) \equiv u_n^{out}(z, t))$ and incoming $(u_n(z, t) \equiv u_n^{inc}(z, t))$ waves on the virtual boundaries $\mathbf{L_m}$ in the semi-infinite waveguides (waveguide ports) with numbers $m = 1, 2$. The upper sign here corresponds to waves propagating towards increasing z and the lower sign towards decreasing z. The final line presents a generalized EAC formulation for the rectangular virtual boundary $\mathbf{L}$, which confines the entire analysis domain $\mathbf{Q_L}$. All physical quantities in (1) have dimensions of SI (the International System of Units) except the time variable t that is the product of the true time t' and the speed of light in vacuum c: $t = ct'$ ($c = 299\,792\,458$ m/s), thus t is measured in meters. Furthermore, $\mu_n(y) = \sqrt{2/a}\sin(\lambda_n(y - y_0))$ is the orthonormal system of transverse functions of plane-parallel waveguides; $\lambda_n = n\pi/a$ are their eigen numbers; $a = y_1 - y_0$ is the waveguides' width (it is the same for all waveguides in this work); y_0 and y_1 are the coordinates of waveguide walls; ε and μ represent the relative permittivity and permeability; η_0 denotes the free space impedance; $K_n(t) = J_1(\lambda_n t)/t$, $J_1(t)$ is the Bessel function.

The operator $\mathbf{A_L}$ represents the EAC for the rectangular virtual boundary $\mathbf{L}$. This EAC is formulated for E_x component of the outgoing field on this boundary. It is obtained as the solution to the following auxiliary initial boundary value problems on each rectilinear fragment of $\mathbf{L}$ [27, 28]:

$$
\begin{cases}
E_x(y, z_i, t) = -\dfrac{2}{\pi}\int\limits_0^{\pi/2} \dfrac{\partial V_z}{\partial t}d\varphi, \\
\dfrac{\partial^2 V_z}{\partial t^2} - \sin^2\varphi \dfrac{\partial^2 V_z}{\partial y^2} = \pm\dfrac{\partial E_x}{\partial z}, \quad \begin{Bmatrix} z_i = Z \\ z_i = 0 \end{Bmatrix}, \\
V_z\big|_{t=0} = \partial V_z/\partial t\big|_{t=0} = 0
\end{cases}
\tag{2}
$$

$$
\begin{cases}
E_x(y_i, z, t) = -\dfrac{2}{\pi}\int\limits_0^{\pi/2} \dfrac{\partial V_y}{\partial t}d\varphi, \\
\dfrac{\partial^2 V_y}{\partial t^2} - \sin^2\varphi \dfrac{\partial^2 V_y}{\partial z^2} = \pm\dfrac{\partial E_x}{\partial y}, \quad \begin{Bmatrix} y_i = Y \\ y_i = 0 \end{Bmatrix}, \\
V_y\big|_{t=0} = \partial V_y/\partial t\big|_{t=0} = 0.
\end{cases}
\tag{3}
$$

Here, $V_y = V_y(z, t, \varphi; y_i)$ and $V_z = V_z(y, t, \varphi; z_i)$ are auxiliary functions; y_i and z_i are parameters specifying the rectilinear section of the virtual boundary on which the associated function is defined. At the corner points of the boundary **L**, the functions V_y and V_z are coupled by the relations

$$
\begin{cases}
\dfrac{\partial V_z}{\partial t} + \sin\varphi \dfrac{\partial V_z}{\partial y} = \mp \displaystyle\int_0^{\pi/2} R(\varphi, \varphi') \dfrac{\partial V_y}{\partial z} d\varphi' \left\{ \begin{matrix} z=Z \\ z=0 \end{matrix} \right\}, \\[3mm]
\dfrac{\partial V_y}{\partial t} + \sin\varphi \dfrac{\partial V_y}{\partial z} = \mp \displaystyle\int_0^{\pi/2} R(\varphi, \varphi') \dfrac{\partial V_z}{\partial y} d\varphi' \left\{ \begin{matrix} y=Y \\ y=0 \end{matrix} \right\},
\end{cases}
\tag{4}
$$

where

$$
R(\varphi, \varphi') = \frac{\sin^2 \varphi'}{\sin^2 \varphi + \sin^2 \varphi' \cos^2 \varphi}.
\tag{5}
$$

Discretization of the initial-boundary value problems (1)–(5) in the framework of a standard explicit FDTD scheme (second-order accuracy with stepwise approximation of physical boundaries [33]) allows us to compute their solutions in the time domain under the excitation by a pulsed wave $u_n^{inc}(z, t)\big|_{\mathbf{L}_m}$ emanating from any waveguide port. Below we restrict ourselves to the case of excitation by waves of the port **I** ($m = 1$). The time profile of $u_n^{inc}(z, t)\big|_{\mathbf{L}_1}$ can be selected freely. We employ two types of sources.

The first source

$$
u_n^{inc}(z, t) = S(t) \cdot \cos(k_c(t - T)),
\tag{6}
$$

where

$$
S(t) = x^2(t) \cdot (3 - 2x(t)),
$$

$$
x(t) = \begin{cases}
(t - t_0)/(t_1 - t_0), & t_0 \le t \le t_1 \\
1, & t_1 < t < t_2 \\
(t - t_3)/(t_2 - t_3), & t_2 \le t \le t_3 \\
0, & t < 0, \ t > t_3
\end{cases},
$$

is relatively narrowband, with its spectrum $\widetilde{u}_n^{inc}(z, k)$ concentrated around the carrier k_c. This source is utilized to compute characteristics of the objects under investigation at a specific fixed frequency.

The second source

$$
u_n^{inc}(z, t) = 4 \cdot S(t) \cdot \cos(k_c(t - T)) \frac{\sin(k_s(t - T))}{t - T}
\tag{7}
$$

is relatively broadband, with its spectrum $\widetilde{u}_n^{inc}(z, k)$ primarily concentrated in the band $k_c - k_s < k < k_c + k_s$, where its amplitude approaches 1 and diminishes to 0 outside this band. This source is utilized with $T = t_1 = t_2 = (t_0 + t_3)/2$ to compute characteristics across a frequency band.

Throughout this work, the time-domain wave $u(t)$ and its frequency-domain counterpart $\widetilde{u}(k)$ are linked via the Fourier transform:

$$
\widetilde{u}(k) = (2\pi)^{-1} \int_{-\infty}^{\infty} u(t) e^{ikt} dt.
\tag{8}
$$

In addition to the electromagnetic field patterns, which are obtained solving the problems (1)–(5) numerically, we also consider the following characteristics [18, 27].

- Frequency-dependent reflection ($R(k)$) and transmission ($T(k)$) coefficients of the incoming (from the port **I**) TE_1-wave into TE_1-waves reflected back into the port **I** and transmitted into the port **II**, respectively. They are calculated as

$$
R_n(k) = \frac{\left| \widetilde{u}_n^{out,1}(z_1, k) \right|^2}{\left| \widetilde{u}_n^{inc,1}(z_1, k) \right|^2}, \quad T_n(k) = \frac{\left| \widetilde{u}_n^{out,2}(z_2, k) \right|^2}{\left| \widetilde{u}_n^{inc,1}(z_1, k) \right|^2}.
\tag{9}
$$

Here, z_1 and z_2 are longitudinal coordinates on the virtual boundaries in the corresponding waveguide ports. Further, only the fundamental modes ($n = 1$) of the waveguide ports will be considered, so the following notations $R \equiv R_1$ and $T \equiv T_1$ are used.

- Far-field radiation pattern

$$
D(\phi, k) = \lim_{r \to \infty} \frac{\left| \widetilde{E}_x(r, \phi, k) \right|^2}{\max\limits_{0 \le \phi \le 2\pi} \left| \widetilde{E}_x(r, \phi, k) \right|^2}.
\tag{10}
$$

This limit is calculated using the asymptotic representation of the Hankel function $H_m^{(1)}(\cdots)$ in the expansion $\widetilde{E}_x(r, \phi, k) = \sum_{m=-\infty}^{m=\infty} a_m(k) H_m^{(1)}(kR) e^{im\phi}$ in terms of angular harmonics of the electric field on the reference circle **R** (Fig. 2) [27]. The angle ϕ is measured counterclockwise from the axis z as shown in Fig. 2.

3. MODEL OF THE OPEN RESONATOR

3.1. Antenna

The design process of the OR commences with the consideration of the diffraction radiation antenna shown in Fig. 3. It consists of two semi-infinite plane-parallel waveguides with width a, interconnected by a segment of a dielectric waveguide with width a_1 and permittivity ε_1. A reflective diffraction grating is positioned in the near field of this dielectric waveguide. The grating acts as a frequency-selective element, ensuring the transformation of surface waves of the dielectric waveguide into bulk waves and their frequency-angular selection [15, 16, 27]. Stringent requirements are imposed on such a grating: aside from the directional radiation at the resonant
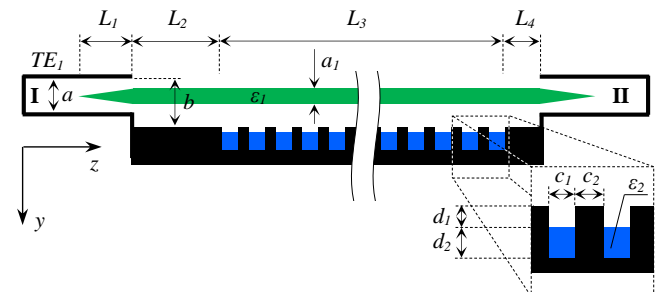
FIGURE 3. Diffraction radiation antenna with reflective diffraction grating and two identical waveguide ports.

frequency, it should minimize radiation at other frequencies. Otherwise, standing waves with nonspecular reflection from the grating may appear in the resonator.

Extensive numerical experiments have shown that they could be numerous enough to cause the resonator to lose its frequency-selective property in certain frequency ranges. One approach to constructing a grating that meets these criteria is to enhance the Q factor of oscillations excited in each groove of the grating. This is achieved by partially filling the grooves with a dielectric material. In this case, both the groove itself and its filling have a rectangular shape, effectively forming an elementary resonator. This resonator consists of a segment of a plane-parallel waveguide filled with a dielectric material, bounded on one side by a metal wall and on the other side by a segment of a beyond cutoff (at the resonant frequency) plane-parallel waveguide with the length d_1 (Fig. 3). It is possible to control the Q factor of the operating oscillation of the elementary resonator by adjusting its geometric parameters d_1, d_2, and c_1 (Fig. 3), thereby achieving the required energy characteristics of the entire antenna.

Let us set the width of the plane-parallel waveguide as $a = 7.11$ mm, which corresponds to the wide wall of the rectangular waveguide WR28 with 7.11 mm × 3.56 mm cross-section. Its first two cutoff wavenumbers are $\widetilde{k}_1^{cut} = 441.856$ m^{-1} and $\widetilde{k}_2^{cut} = 883.711$ m^{-1}, i.e., the frequency range where only one propagating mode exists spans from 21.082 GHz to 42.165 GHz. It falls within the Ka band. The parameters of the dielectric waveguide are specified as follows: width $a_1 = 0.4a$, permittivity $\varepsilon_1 = 2.1$ (corresponds to that of Teflon), and length of the wedge-shaped matching sections $L_1 = a$. Considering this particular waveguide configuration with a flat metal substrate (without diffraction grating), in the proximity of the assumed resonant frequency (approximately at $820 < k < 860$ m^{-1}, as detailed below), we observe that over 98% of the input energy is transmitted from port **I** to port **II**, about 1.5% of the energy radiated, and less than 0.5% reflected back to port **I**.

We conducted a heuristic search to determine the parameters d_1, d_2, c_1 (which define the resonant frequency, the Q factor of oscillations in the grating cells, and the width of spectral line of the operating oscillation), b (which determines the radiation level, primarily at non-resonant frequencies), c_2 (which sets the radiation angle ϕ), and N (the number of the grating grooves that specify the total length of the grating L_3 and the portion of radiated energy). The permittivity of the fillings in the grating grooves is assumed to be $\varepsilon_2 = 3.8$ (corresponds to that of quartz). Below, we present the results of the model synthesis of the OR for the most interesting set of the parameters' values, namely, $b = 1.05a$, $c_1 = 0.3a$, $c_2 = 0.2a$, $d_1 = 0.2a$, $d_2 = 0.5a$, and $N = 50$ (which makes $L_3 = 176.328$ mm). Other geometric parameters are set as $L_2 = 263.07$ mm, $L_4 = 58.302$ mm, and $L_2 + L_3 + L_4 = 497.7$ mm.

The studied range $480 \leq k \leq 960$ m^{-1} is one octave wide and slightly above the cutoff frequency of the fundamental mode of the feeding waveguide. First, we excite the structure with the wideband source (7) with the following values of its parameters: $k_c = 720$ m^{-1}, $k_s = 240$ m^{-1}, $t_0 = 0$, and $t_3 =$
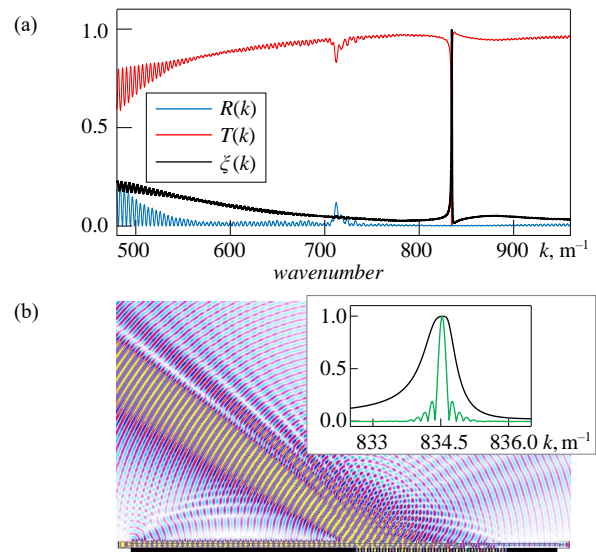

FIGURE 4. Spatial and frequency characteristics of the antenna from Fig. 3: (a) coefficients of reflection $R(k)$ (back into port **I**), transmission $T(k)$ (from port **I** to port **II**), and radiation ($\xi(k) = 1 - R(k) - T(k)$); (b) field pattern of $E_x(g, t)$ component at the moment of time $t = 30$ m under the narrowband excitation by pulse (6) with $k_c = 834.535$ m^{-1}; (inset) spectrum of the narrowband excitation pulse (green line) in the vicinity of maximum of the radiation coefficient $\xi(k)$ (black line).

0.4 m. Fig. 4(a) plots the coefficients of transmission $T(k)$, reflection $R(k)$, and radiation $\xi(k) = 1 - R(k) - T(k)$. The curve

$\xi(k)$ has a pronounced resonant peak at $\widetilde{k}_0 \approx 834.535$ m^{-1}. Next, we excite the structure with the narrowband pulse (6) with the carrier $k_c = \widetilde{k}_0$ and $t_0 = 0$, $t_1 = 10$ m, $t_2 = 40$ m, $t_3 = 50$ m. Fig. 4(b) illustrates the field pattern of E_x component within the analysis domain at the moment of time $t = 30$ m under this excitation. In the inset of Fig. 4(b), the spectrum of excitation pulse (6) is plotted alongside the radiation $\xi(k)$. The field pattern provides a preliminary insight into the characteristics of the frequency-angle selection of this antenna near the resonant frequency and the formation of its radiation pattern. More detailed information can be obtained by computing the radiation pattern itself.

To achieve this, we modify the antenna to the form in which it will be integrated into the synthesized resonator (Fig. 5(a)). We remove the waveguide port **II** from the structure to allow radiation into free space through that end of the waveguide. Additionally, we add a beyond cutoff diaphragm to port **I**, which will function as a mirror for a standing wave within the resonator and facilitate energy exchange with port **I**. The diaphragm parameters are $d_3 = 1.5a$, $d_4 = 0.2a$, and its thickness is $0.05a$; the open line parameters are $L_1 = 1.75a$, $L_2 = 37a$, $L_4 = 8.25a$.

Fig. 5(b) shows the radiation pattern of the modified antenna within the studied frequency range. As anticipated, at non-resonant frequencies, nearly all the energy received through the diaphragm is radiated at small angles ($\phi < 40°$). In the vicinity of the resonant frequency, the situation differs significantly, namely, a substantial portion of the energy (more than 98% near
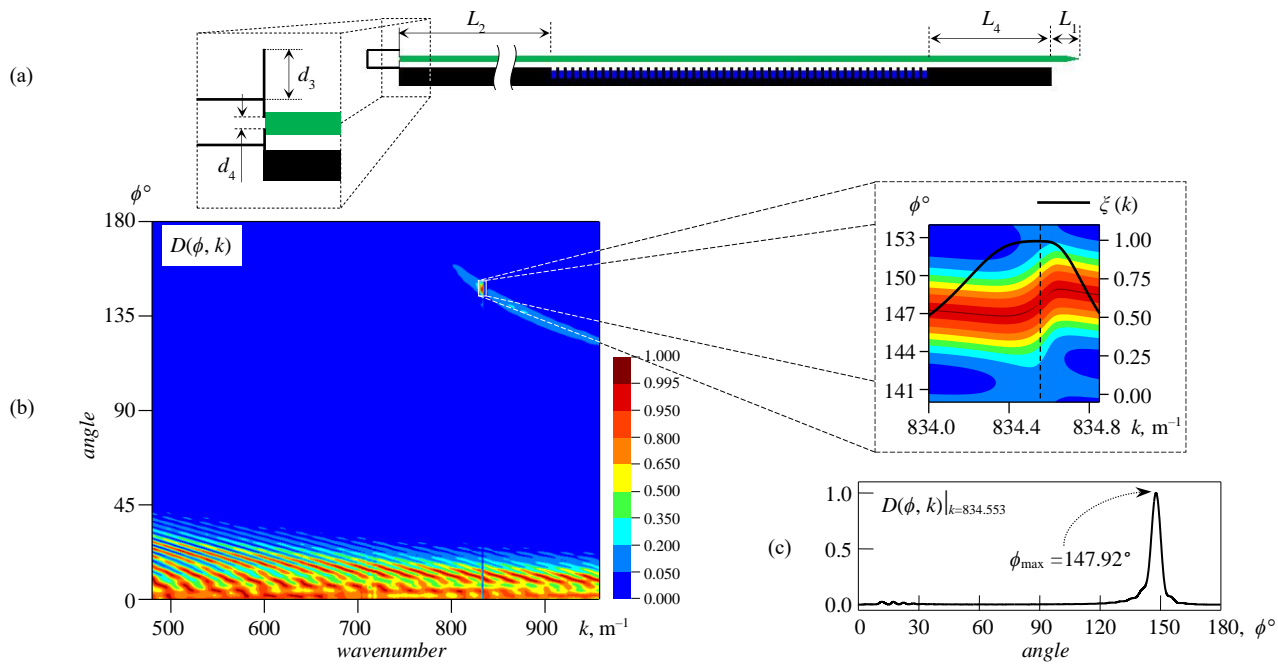
FIGURE 5. Modified antenna with diffraction grating and diaphragm (a), its radiation pattern within the frequency range (b) and for the wavenumber $\widetilde{k}_1 = 834.553\,\mathrm{m}^{-1}$ (c).

$\widetilde{k}_0$) is radiated within the angular range $144° < \phi < 152°$, see Fig. 5(b). In this scenario, the function $\phi_{max}(k)$ (representing the frequency dependence of the main lobe's direction) has its derivative's sign changed near the resonance. This observation prompts us to refine the resonant frequency, setting it as the midpoint of the frequency range where this derivative is positive. This frequency corresponds to $\widetilde{k}_1 \approx 834.553\,\mathrm{m}^{-1}$, which is marked in the inset of Fig. 5(b) with a dashed line. A fragment of the radiation $\xi(k)$ is also plotted (solid line, right scale). Fig. 5(c) illustrates the radiation pattern at $\widetilde{k}_1$, with its maximum directed at $\phi_{max} = 147.92°$.

3.2. Resonator

Now we can assemble the resonator as a whole. For it, a flat mirror is placed at the angle $\alpha = \phi_{\max} - 90° = 57.92°$ to the axis z, as shown in Fig. 6(a). We consider three OR configurations with different grating-to-mirror distances, Fig. 6(b). It is evident that OR synthesis requires precise tuning to the resonant frequency. A straightforward solution to this challenge is to move the flat mirror, i.e., vary the parameters L_6 and d_5. A more elegant solution is to move the diffraction grating along the axis z, i.e., vary the parameter L_2 (see Fig. 5(a)).

TABLE 1. Parameters of three configurations of the open resonators.

	L_6	d_5	L_2	$\widetilde{k}_{res}$	Q
Resonator#1	0	$27.10a$	$47.55a$	834.575	18 000
Resonator#2	$18.75a$	$15.30a$	$47.50a$	834.580	14 700
Resonator#3	$37.55a$	$3.50a$	$47.50a$	834.540	12 300

We have employed both of these configuration-tuning methods. Table 1 presents geometric parameters for three OR configurations, their resonance wavenumbers $\widetilde{k}_{res}$, and Q factors of operating oscillations. Q factors are calculated by estimating the resonance duration for a freely oscillating field. The normalized amplitude spectra of the E_x component at the observation points P_0 and P_1, when these ORs are excited with the TE_1 wave (7) with $k_c = 720\,\mathrm{m}^{-1}$, $k_s = 240\,\mathrm{m}^{-1}$, $t_0 = 0$, $t_3 = 0.4\,\mathrm{m}$, are depicted in Fig. 6(c) and Fig. 6(d). The point P_0 is positioned at the distance $0.28a$ (approximately quarter of the resonant frequency wavelength) from the mirror's surface and at the distance $L_7 = 6.56a$ from its lower edge. The point P_1 is located in the middle of the cross-section of the dielectric waveguide at the distance $L_5 = 22.7a$ from the diaphragm.

It is evident that one frequency predominates in the spectral composition of the field within the resonator. In its immediate vicinity, there is a non-resonant background. At these non-resonant frequencies, the field amplitude is ten times lower than at the resonant one. The standing wave of the operating oscillation comprises two components, namely, one within the dielectric waveguide (with 114 electric field antinodes) and the other in the space between the mirror and the grating (with 113 electric field antinodes at the closest distance to the nearest grating groove for Resonator# 1). The latter exhibits a rather complex structure and clearly defined directions of the field radiation from the OR into open space. Despite this radiation, the operating oscillation maintains a sufficiently high Q factor of $Q > 12000$.

The field spectra at the point P_1 (Fig. 6(d)) exhibit a resonant peak on a pedestal. This pedestal appears due to the partial transfer of the energy of excitation through the diaphragm. This process is fundamentally non-resonant, and the portion of
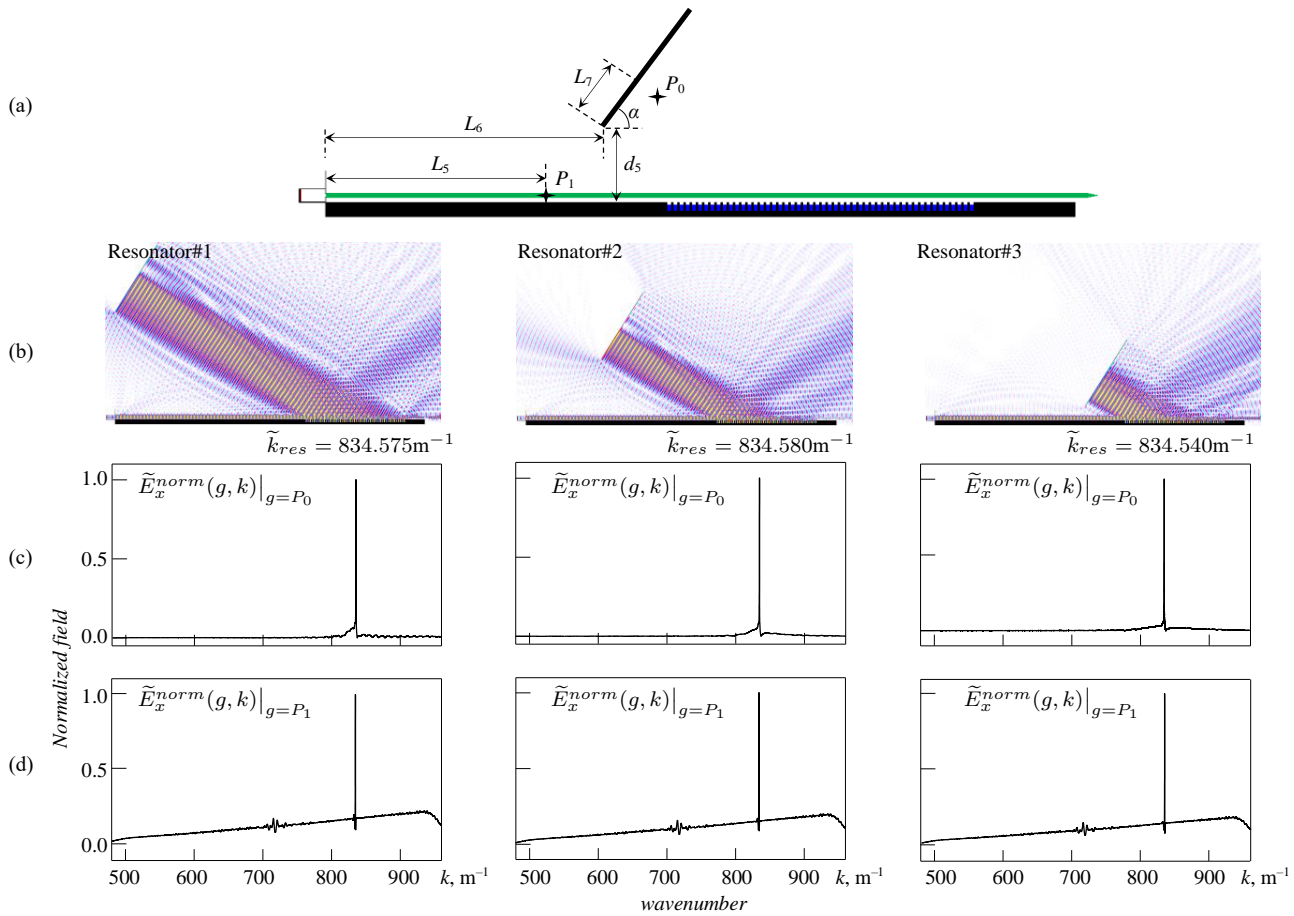
FIGURE 6. The schematic of the ORs (a) and the spatial-frequency characteristics of three ORs with different distances from the plane mirror to the diffraction grating: the distribution of the electric field component $E_x(g)$ in the computational domain in the steady state (b) and the normalized field amplitude spectrum $\widetilde{E}_x^{norm}(k)$ at the observation point P_0 (c) and P_1 (d). The geometrical parameters are given in the text.

transmitted energy depends solely on the ratio of the diaphragm size d_4 (Fig. 5(a)) to the wavelength. Reducing d_4 allows for a substantial reduction in the portion of the energy entering the resonator in a non-resonant way, consequently decreasing this pedestal's height.

For comparison, Fig. 7 presents the geometry and transmission coefficient $T(k)$ of a waveguide-type OR. This OR is constructed from a segment of the same dielectric waveguide as used earlier, which is positioned over a flat metal substrate and constrained by two diaphragms identical to those employed in the OR discussed above. The distance $L = 47.5a$ coincides with L_2 in the second and third resonators (see Table 1). Essentially, this illustrates the efficacy of the proposed technique for thinning of the OR eigenfrequency spectrum. To be exact, augmenting the structure depicted in Fig. 7(a) with the "diffraction grating — flat mirror" system allows to preserve just one high-Q oscillation instead of 77 shown in Fig. 7(b).

Another crucial feature of the proposed resonator design must be emphasized. Namely, dimensions of this resonator could be significantly increased. This expansion can be achieved by enlarging the gap between the mirror and the diffraction grating or the distance between the grating and the diaphragm. The first approach has limitations imposed
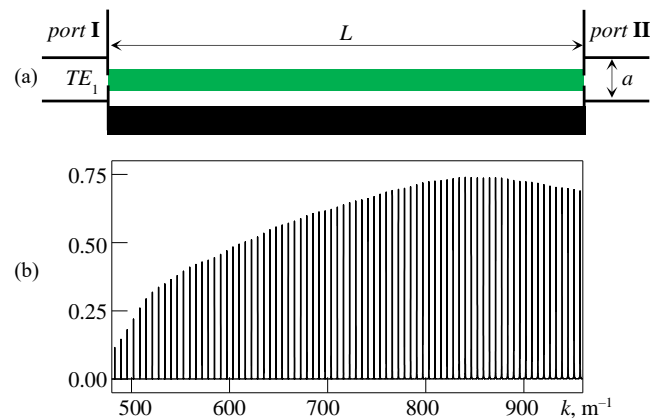

FIGURE 7. Geometry of waveguide resonator without grating and mirror (a) and its coefficient of transmission from port **I** to port **II** (b).

by radiation losses. Although the data presented in Table 1 suggests a reverse trend (decrease in Q factor of the operating oscillation as the mirror approaches the grating), this effect is local in nature. At sufficiently large distances between the mirror and the grating, the increase in losses will surpass the growth of stored energy, naturally limiting the resonator's

size. The second approach is more attractive since radiation losses in a conventional dielectric waveguide are considerably lower than in the energy propagation between the mirror and the grating. By adopting this approach, we can create resonator configurations with a rather extended waveguide segment, concentrating most of the standing wave energy, and a relatively small space between the mirror and the grating. In this scenario, the grating acts as an interference reflector, efficiently reflecting the waveguide modes within a narrow frequency band.

4. CONCLUSION

We have proposed a model of a quasi-optical open resonator with one dominant eigen oscillation (it is characterized by a high quality factor of $Q > 10^4$) within the operating frequency band of approximately one octave. The resonator is created by combining a diffraction radiation antenna with a flat metal mirror, allowing efficient energy output to a waveguide of standard cross-section. The longitudinal size of the resonator exceeds the wavelength of the operating oscillation by more than 50 times. Owing to constructive features of the resonator, a change in its dimensions affects only the longitudinal index of the operating oscillation. This design flexibility suggests the potential for further increase of resonator's size relative to the operating wavelength. The presented resonator, designed for use in the Ka band, can be scaled to other frequency ranges with minimal modifications using the proposed model synthesis technique.

ACKNOWLEDGEMENT

REFERENCES

[1] Fouckhardt, H., A.-K. Kleinschmidt, J. Strassner, and C. Doering, "1D confocal broad area semiconductor lasers (Confocal BALs) for fundamental transverse mode selection (TMS#0)," *Advances in OptoElectronics*, Vol. 2019, 1–7, Jun. 2019.

[2] Duchiron, G., D. Cros, P. Guillon, M. Chaubet, and C. Zanchi, "Mode selection for a whispering gallery mode resonator," in *29th European Microwave Conference*, 44–46, Munich, Germany, 1999.

[3] Di Monaco, O., W. Daniau, I. Lajoie, Y. Gruson, M. Chaubet, and V. Giordano, "Mode selection for a whispering gallery mode resonator," *Electronics Letters*, Vol. 32, No. 7, 669–670, 1996.

[4] Levitskii, I. and V. Evtikhiev, "Mode selection control in microring resonators," *Journal of Physics: Conference Series*, Vol. 769, 1–5, 2016.

[5] Pazynin, V., "Sparseness of natural oscillations spectrum for double-mirror open resonator using mode-selective scatterers on one of mirrors surface," *Radioelectronics and Communication Systems*, Vol. 64, 525–534, 2021.

[6] Raskhodchikov, A., S. Scherbak, N. Kryzhanovskaya, A. Zhukov, and A. Lipovskii, "Dielectric surrounding decimates eigenmodes of microdisk optical resonators," *Journal of Physics: Conference Series*, Vol. 1124, 1–4, 2018.

[7] Ilchenko, S., R. Lymarenko, V. Taranenko, N. Kyzas, and A. Belosludtsev, "Multilayer dielectric structure for mode selection of wide-aperture laser," in *IEEE 8th International Conference Advanced Optoelectronics and Lasers (CAOL)*, 1–4, Sozopol, Bulgaria, Sept. 2019.

[8] Yang, Z., J. Leger, and A. Shchegrov, "Three-mirror resonator with aspheric feedback mirror for laser spatial mode selection and mode shaping," *Journal of Physics: Conference Series*, Vol. 40, 1258–1269, Sept. 2004.

[9] Serkland, D., H. So, G. Peake, M. Wood, A. Grine, C. Hains, K. Geib, and G. Keeler, "Mode selection and tuning of single-frequency short-cavity VECSELs," in *Proc. SPIE OPTO Vertical-Cavity Surface-Emitting Lasers XXII*, Vol. 10552, San Francisco, USA, 2018.

[10] Buttner, A., R. Kowarschik, and U. Zeitner, "Folded diffractive laser resonators with user-defined fundamental mode," *Applied Physics B*, Vol. 81, 601–606, Sept. 2005.

[11] Ostroukh, O., R. Lymarenko, and V. Taranenko, "Model of wide-aperture laser with intracavity diffractive element," in *IEEE 8th International Conference Advanced Optoelectronics and Lasers (CAOL)*, 188–191, Sozopol, Bulgaria, Sept. 2019.

[12] Ginzburg, N., A. Sergeev, E. Kocharovskaya, A. Malkin, E. Egorova, and V. Zaslavsky, "Diffraction mode selection in planar Bragg resonators of optical and microwave wavelength ranges," *Physics Letters A*, Vol. 384, No. 10, 1–5, Apr. 2020.

[13] Ginzburg, N., A. Sergeev, E. Kocharovskaya, A. Malkin, E. Egorova, and V. Zaslavsky, "Diffraction-mode selection in heterolasers with planar Bragg structures," *Semiconductors*, Vol. 54, 1161–1165, Sept. 2020.

[14] Zapevalov, V., S. Vlasov, E. Koposova, A. Kuftin, A. Paveliev, and N. Zavolsky, "Various types of echelette resonators for gyrotrons," in *EPJ Web of Conferences*, Vol. 195, Nizhny Novgorod, Russia, Oct. 2018.

[15] Shestopalov, V., *The Smith-Purcell Effect*, Nova Science Publishers, 1998.

[16] Sautbekov, S., K. Sirenko, Y. Sirenko, and A. Yevdokymov, "Diffraction radiation effects: A theoretical and experimental study," *IEEE Antennas and Propagation Magazine*, Vol. 57, No. 5, 73–93, Oct. 2015.

[17] Sirenko, Y., S. Sautbekov, N. Yashina, and K. Sirenko, "Diffraction radiation generated by a density-modulated electron beam flying over the periodic boundary of the medium section. I. Analytical basis," *Progress In Electromagnetics Research B*, Vol. 91, 1–8, 2021.

[18] Sirenko, Y., S. Sautbekov, N. Yashina, and K. Sirenko, "A new approach to formation and directed radiation of powerful short radio pulses," *IEEE Transactions on Plasma Science*, Vol. 50, No. 10, 3422–3433, 2022.

[19] Yevdokymov, A. and V. Kryzhanovskiy, "Diffraction radiation antennas for SHF and EHF radiosystems," in *6th International Conference on Antenna Theory and Techniques*, 59–64, Sevastopol, Ukraine, Sept. 2007.

[20] Melezhik, P., Y. Sidorenko, S. Provalov, S. Andrenko, and S. Shilo, "Planar antenna with diffraction radiation for radar complex of millimeter band," *Radioelectronics and Communication Systems*, Vol. 53, 233–240, 2010.

[21] Shylo, S., Y. Sydorenko, D. Wheeler, and D. Dundonald, "A W-band passive imaging system implemented with rotating diffraction antenna technology," in *Millimetre Wave and Terahertz Sensors and Technology VI*, Vol. 8900, 36–45, Dresden, Germany, 2013.

[22] Sirenko, K., Y. Sirenko, and A. Yevdokymov, "Diffraction antennas. Planar structures with controllable beam positioning," *Telecommunications and Radio Engineering*, Vol. 78, No. 10, 835–851, 2019.

[23] Sirenko, Y. and A. Yevdokymov, "Diffraction antennas. Linear structures on the basis of a ridged waveguide," *Telecommunications and Radio Engineering*, Vol. 77, No. 14, 1203–1229, 2018.

[24] Sirenko, Y., S. Sautbekov, M. Sautbekova, N. Yashina, N. Burambayeva, and A. Begimova, "Axial-symmetric diffraction radiation antenna with a very narrow funnel-shaped directional diagram," *Applied Sciences*, Vol. 11, No. 21, 10381, Nov. 2021.

[25] Sidorenko, Y., S. Provalov, S. Shylo, and D. Wheeler, "Compact MMW-band planar diffraction type antennas for various applications," *American Journal of Electromagnetics and Applications*, Vol. 8, No. 1, 18–27, Jun. 2020.

[26] Perov, A., Y. Sirenko, and N. Yashina, "Explicit conditions for virtual boundaries in initial boundary value problems in the theory of wave scattering," *Journal of Electromagnetics and Applications*, Vol. 13, No. 10, 1343–1371, 1999.

[27] Sirenko, Y. and L. Velychko (eds.), *Electromagnetic Waves in Complex Systems: Selected Theoretical and Applied Problems*, Springer, 2016.

[28] Sirenko, Y., V. Pazynin, K. Sirenko, and N. Yashina, "Exact absorbing conditions for initial boundary value problems of computational electrodynamics. Review," Chapter 3 in *A Closer Look at Boundary Value Problems,* M. Avci (ed.), 43–124, Nova Science Publishers, 2020.

[29] Sirenko, K., V. Pazynin, Y. Sirenko, and H. Bagci, "An FFT-accelerated FDTD scheme with exact absorbing conditions for characterizing axially symmetric resonant structures," *Progress In Electromagnetics Research*, Vol. 111, 331–364, 2011.

[30] Pazynin, V., "Simulation of the characteristics of an active microwave power compressor," *Telecommunications and Radio Engineering*, Vol. 76, No. 12, 1033–1047, 2017.

[31] Pazynin, V., S. Sautbekov, K. Sirenko, Y. Sirenko, A. Vertiy, and N. Yashina, "Comparison of exact and approximate absorbing conditions for initial-boundary value problems of the electromagnetic theory of gratings," *Telecommunications and Radio Engineering*, Vol. 77, No. 18, 1581–1595, 2018.

[32] Sirenko, K., M. Liu, and H. Bagci, "Incorporation of exact boundary conditions into a discontinuous Galerkin finite element method for accurately solving 2D time-dependent Maxwell equations," *IEEE Transactions on Antennas Propagation*, Vol. 61, No. 1, 472–477, Jan. 2013.

[33] Taflove, A. and S. Hagness, *Computational Electrodynamics: The Finite-Difference Time-Domain Method*, Artech House, 2005.